

Updated High-Temperature Opacities for The Dartmouth Stellar Evolution Program and their Effect on the Jao Gap Location

2 THOMAS M. BOUDREAUX¹ AND BRIAN C. CHABOYER¹

3 *¹Department of Physics and Astronomy, Dartmouth College, Hanover, NH 03755, USA*

4 ABSTRACT

5 The Jao Gap, a 17 percent decrease in stellar density at $M_G \sim 10$ identified in both Gaia DR2
6 and EDR3 data, presents a new method to probe the interior structure of stars near the fully con-
7 vective transition mass. The Gap is believed to originate from convective kissing instability wherein
8 asymmetric production of ^3He causes the core convective zone of a star to periodically expand and
9 contract and consequently the stars' luminosity to vary. Modeling of the Gap has revealed a sensitivity
10 in its magnitude to a population's metallicity primarily through opacity. Thus far, models of the Jao
11 Gap have relied on OPAL high-temperature radiative opacities. Here we present updated synthetic
12 population models tracing the Gap location modeled with the Dartmouth stellar evolution code using
13 the OPLIB high-temperature radiative opacities. Use of these updated opacities changes the predicted
14 location of the Jao Gap by ~ 0.05 mag as compared to models which use the OPAL opacities. This
15 difference is likely too small to be detectable in empirical data.

16 *Keywords:* Stellar Evolution (1599) — Stellar Evolutionary Models (2046)

17 1. INTRODUCTION

18 Due to the initial mass requirements of the molecular
19 clouds which collapse to form stars, star formation is
20 strongly biased towards lower mass, later spectral class
21 stars when compared to higher mass stars. Partly as
22 a result of this bias and partly as a result of their ex-
23 tremely long main-sequence lifetimes, M Dwarfs make
24 up approximately 70 percent of all stars in the galaxy.
25 Moreover, some planet search campaigns have focused
26 on M Dwarfs due to the relative ease of detecting small
27 planets in their habitable zones (e.g. Nutzman & Char-
28 bonneau 2008). M Dwarfs then represent both a key
29 component of the galactic stellar population as well as
30 the possible set of stars which may host habitable ex-
31 oplanets. Given this key location M Dwarfs occupy in
32 modern astronomy it is important to have a thorough
33 understanding of their structure and evolution.

34 Jao et al. (2018) discovered a novel feature in the Gaia
35 Data Release 2 (DR2) $G_{BP} - G_{RP}$ color-magnitude-
36 diagram. Around $M_G = 10$ there is an approximately

37 17 percent decrease in stellar density of the sample of
38 stars Jao et al. (2018) considered. Subsequently, this
39 has become known as either the Jao Gap, or Gaia M
40 Dwarf Gap. Following the initial detection of the Gap
41 in DR2 the Gap has also potentially been observed in
42 2MASS (Skrutskie et al. 2006; Jao et al. 2018); however,
43 the significance of this detection is quite weak and it re-
44 lies on the prior of the Gap's location from Gaia data.
45 Further, the Gap is also present in Gaia Early Data Re-
46 lease 3 (EDR3) (Jao & Feiden 2021). These EDR3 and
47 2MASS data sets then indicate that this feature is not
48 a bias inherent to DR2.

49 The Gap is generally attributed to convective instabil-
50 ities in the cores of stars straddling the fully convective
51 transition mass (0.3 - 0.35 M_\odot) (Baraffe & Chabrier
52 2018). These instabilities interrupt the normal, slow,
53 main sequence luminosity evolution of a star and result
54 in luminosities lower than expected from the main se-
55 quence mass-luminosity relation (Jao & Feiden 2020).

56 The Jao Gap, inherently a feature of M Dwarf pop-
57 ulations, provides an enticing and unique view into the
58 interior physics of these stars (Feiden et al. 2021). This
59 is especially important as, unlike more massive stars,
60 M Dwarf seismology is infeasible due to the short peri-
61 ods and extremely small magnitudes which both radial
62 and low-order low-degree non-radial seismic waves are

Corresponding author: Thomas M. Boudreax
thomas.m.boudreaux.gr@dartmouth.edu,
thomas@boudreauxmail.com

⁶³ predicted to have in such low mass stars (Rodríguez-
⁶⁴ López 2019). The Jao Gap therefore provides one of the
⁶⁵ only current methods to probe the interior physics of M
⁶⁶ Dwarfs.

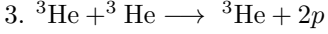
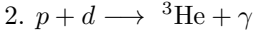
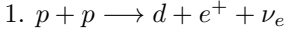
⁶⁷ Despite the early success of modeling the Gap some
⁶⁸ issues remain. Jao & Feiden (2020, 2021) identify that
⁶⁹ the Gap has a wedge shape which has not been successful
⁷⁰ reproduced by any current modeling efforts and which
⁷¹ implies a somewhat unusual population composition of
⁷² young, metal-poor stars. Further, Jao & Feiden (2020)
⁷³ identify substructure, an additional over density of stars,
⁷⁴ directly below the Gap, again a feature not yet fully
⁷⁵ captured by current models.

⁷⁶ All currently published models of the Jao Gap make
⁷⁷ use of OPAL high temperature radiative opacities. Here
⁷⁸ we investigate the effect of using the more up-to-
⁷⁹ date OPLIB high temperature radiative opacities and
⁸⁰ whether these opacity tables bring models more in line
⁸¹ with observations. In Section 2 we provide an overview
⁸² of the physics believed to result in the Jao Gap, in
⁸³ Section 3 we review the differences between OPAL
⁸⁴ and OPLIB and describe how we update DSEP to use
⁸⁵ OPLIB opacity tables. Section 4 walks through the stel-
⁸⁶ lar evolution and population synthesis modeling we per-
⁸⁷ form. Finally, in Section 5 we present our findings.

2. JAO GAP

⁸⁸ A theoretical explanation for the Jao Gap (Figure 1)
⁸⁹ comes from van Saders & Pinsonneault (2012) and Mac-
⁹⁰ Donald & Gizis (2018), who propose that in a star di-
⁹¹ rectly above the transition mass, due to asymmetric pro-
⁹² duction and destruction of ^3He during the proton-proton
⁹³ I chain (ppI), periodic luminosity variations can be in-
⁹⁴ duced. This process is known as convective-kissing in-
⁹⁵ stability. Very shortly after the zero-age main sequence
⁹⁶ such a star will briefly develop a radiative core; however,
⁹⁷ as the core temperature exceeds 7×10^6 K, enough en-
⁹⁸ ergy will be produced by the ppI chain that the core once
⁹⁹ again becomes convective. At this point the star exists
¹⁰⁰ with both a convective core and envelope, in addition
¹⁰¹ to a thin, radiative layer separating the two. Subse-
¹⁰² quently, asymmetries in ppI affect the evolution of the
¹⁰³ star's convective core.

¹⁰⁴ The proton-proton I chain constitutes three reactions



¹⁰⁵ Initially, reaction 3 of ppI consumes ^3He at a slower
¹⁰⁶ rate than it is produced by reaction 2 and as a result,
¹⁰⁷ the core ^3He abundance and consequently the rate of

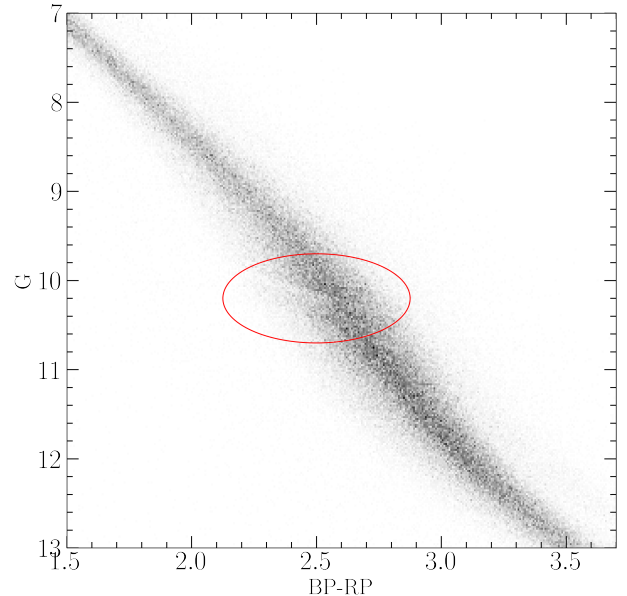


Figure 1. The Jao Gap (circled) seen in the Gaia Catalogue of Nearby Stars (Gaia Collaboration et al. 2021).

¹¹² reaction 3, increases with time. The core convective
¹¹³ zone expands as more of the star becomes unstable to
¹¹⁴ convection. This expansion continues until the core con-
¹¹⁵ nects with the convective envelope. At this point convec-
¹¹⁶ tive mixing can transport material throughout the entire
¹¹⁷ star and the high concentration of ^3He rapidly diffuses
¹¹⁸ outward, away from the core, decreasing energy genera-
¹¹⁹ tion as reaction 3 slows down. Ultimately, this leads to
¹²⁰ the convective region around the core pulling back away
¹²¹ from the convective envelope, leaving in place the radia-
¹²² tive transition zone, at which point ^3He concentrations
¹²³ grow in the core until it once again expands to meet
¹²⁴ the envelope. These periodic mixing events will con-
¹²⁵ tinue until ^3He concentrations throughout the star reach
¹²⁶ an equilibrium ultimately resulting in a fully convective
¹²⁷ star. Figure 2 traces the evolution of a characteristic
¹²⁸ star within the Jao Gap's mass range.

2.1. Efforts to Model the Gap

¹²⁹ Since the identification of the Gap, stellar modeling
¹³⁰ has been conducted to better constrain its location, ef-
¹³¹ fects, and exact cause. Both Mansfield & Kroupa (2021)
¹³² and Feiden et al. (2021) identify that the Gap's mass lo-
¹³³cation is correlated with model metallicity — the mass-
¹³⁴ luminosity discontinuity in lower metallicity models be-
¹³⁵ ing at a commensurately lower mass. Feiden et al. (2021)
¹³⁶ suggests this dependence is due to the steep relation of
¹³⁷ the radiative temperature gradient, ∇_{rad} , on tempera-
¹³⁸ ture and, in turn, on stellar mass.

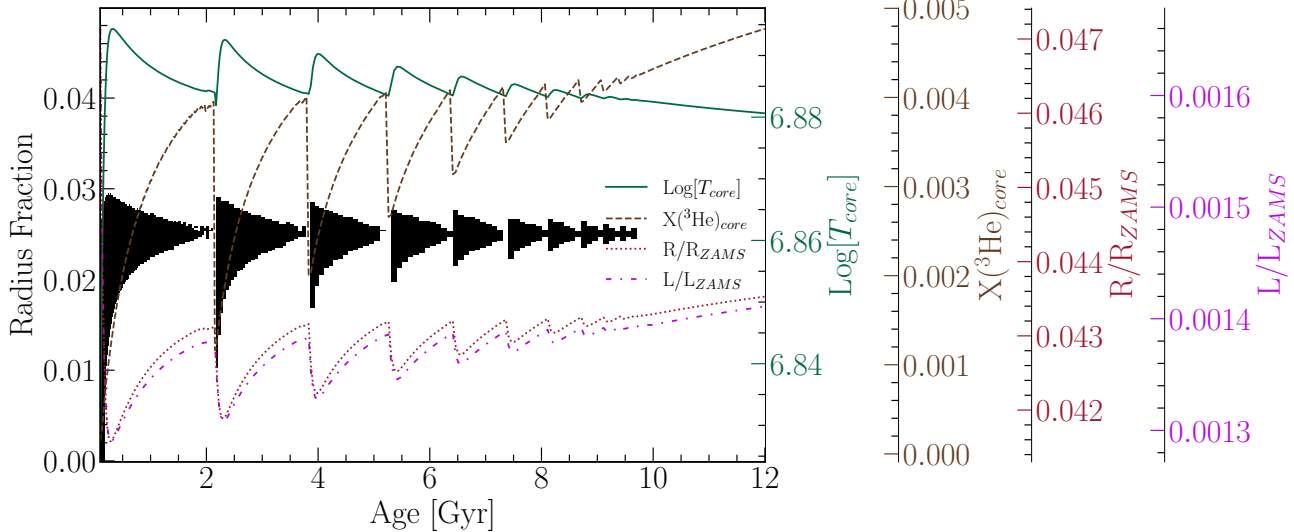


Figure 2. Diagram for a characteristic stellar model of $0.35625 M_{\odot}$ which is within the Jao Gap’s mass range. The black shaded regions denote whether, at a particular model age, a radial shell within the model is radiative (with white meaning convective). The lines trace the models core temperature, core ${}^3\text{He}$ mass fraction, fractional luminosity wrt. the zero age main sequence and fractional radius wrt. the zero age main sequence.

$$\nabla_{rad} \propto \frac{L\kappa}{T^4} \quad (1)$$

As metallicity decreases so does opacity, which, by Equation 1, dramatically lowers the temperature at which radiation will dominate energy transport (Chabrier & Baraffe 1997). Since main sequence stars are virialized the core temperature is proportional to the core density and total mass. Therefore, if the core temperature where convective-kissing instability is expected decreases with metallicity, so too will the mass of stars which experience such instabilities.

The strong opacity dependence of the Jao Gap begs the question: **what is the effect of different opacity calculations on Gap properties.** As we can see above, changing opacity should affect the Gap’s location in the mass-luminosity relation and therefore in a color-magnitude diagram. Moreover, current models of the Gap have yet to locate it precisely in the CMD (Feiden et al. 2021) with an approximate 0.16 G-magnitude difference between the observed and modeled Gaps. Opacity provides one, as yet unexplored, parameter which has the potential to resolve these discrepancies.

3. UPDATED OPACITIES

Multiple groups have released high-temperature opacities including, the Opacity Project (OP Seaton et al. 1994), Laurence Livermore National Labs OPAL opacity tables (Iglesias & Rogers 1996), and Los Alamos National Labs OPLIB opacity tables (Colgan et al. 2016). OPAL high-temperature radiative opacity tables

in particular are very widely used by current generation isochrone grids (e.g. Dartmouth, MIST, & StarEvol, Dotter et al. 2008; Choi et al. 2016; Amard et al. 2019).

OPLIB opacity tables (Colgan et al. 2016) are not widely used but include the most up-to-date plasma modeling.

While the overall effect on the CMD of using OPLIB compared to OPAL tables is small, the strong theoretical opacity dependence of the Jao Gap raises the potential for these small effects to measurably shift the Gap’s location. We update DSEP to use high temperature opacity tables based on measurements from Los Alamos national Labs T-1 group (OPLIB, Colgan et al. 2016). The OPLIB tables are created with ATOMIC (Magee et al. 2004; Hakel et al. 2006; Fontes et al. 2015), a modern LTE and non-LTE opacity and plasma modeling code. These updated tables were initially created in an attempt to resolve the discrepancy between helioseismic and solar model predictions of chemical abundances in the sun (Bahcall et al. 2005).

OPLIB tables include monochromatic Rosseland mean opacities — composed from bound-bound, bound-free, free-free, and scattering opacities — for elements hydrogen through zinc over temperatures 0.5eV to 100 keV (5802 K – $1.16 \times 10^9\text{ K}$) and for mass densities from approximately 10^{-8} g cm^{-3} up to approximately 10^4 g cm^{-3} (though the exact mass density range varies as a function of temperature).

DSEP ramps the Ferguson et al. (2005) low temperature opacities to high temperature opacities tables between $10^{4.3}\text{ K}$ and $10^{4.5}\text{ K}$; therefore, only differences between high-temperature opacity sources above $10^{4.3}$

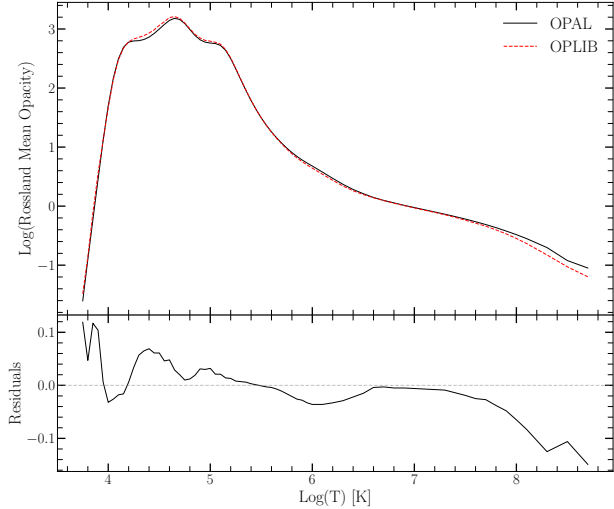


Figure 3. Rosseland mean opacity with the GS98 solar composition for both OPAL opacities and OPLIB opacities (top). Residuals between OPLIB opacities and OPAL opacities (bottom). These opacities are plotted at $\log_{10}(R) = -1.5$, $X = 0.7$, and $Z = 0.02$. Note how the OPLIB opacities are systematically lower than the OPAL opacities for temperatures above 10^5 K.

K can effect model evolution. When comparing OPAL and OPLIB opacity tables (Figure 3) we find OPLIB opacities are systematically lower than OPAL opacities for temperatures above 10^5 K. Between $10^{4.3}$ and 10^5 K OPLIB opacities are larger than OPAL opacities. These generally lower opacities will decrease the radiative temperature gradient throughout much of the radius of a model.

3.1. Table Querying and Conversion

The high-temperature opacity tables used by DSEP and most other stellar evolution programs give Rosseland-mean opacity, κ_R , along three dimensions: temperature, a density proxy R (Equation 2; $T_6 = T \times 10^{-6}$, ρ is the mass density), and composition.

$$R = \frac{\rho}{T_6^3} \quad (2)$$

OPLIB tables may be queried from a web interface¹; however, OPLIB opacities are parametrized using mass-density and temperature instead of R and temperature. It is most efficient for us to convert these tables to the OPAL format instead of modifying DSEP to use the OPLIB format directly. In order to generate many tables easily and quickly we develop a web scraper

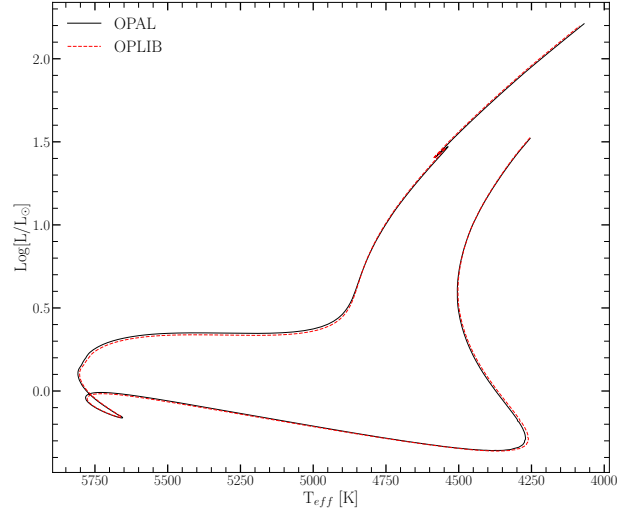


Figure 4. HR Diagram for the two SCSMs, OPAL and OPLIB. OPLIB is shown as a red dashed line.

(pyTOPSScrape, Boudreux 2022) which can automatically retrieve all the tables needed to build an opacity table in the OPAL format. pyTOPSScrape² has been released under the permissive MIT license with the consent of the Los Alamos T-1 group. For a detailed discussion of how the web scraper works and how OPLIB tables are transformed into a format DSEP can use see Appendices A & B.

3.2. Solar Calibrated Stellar Models

In order to validate the OPLIB opacities, we generated a solar calibrated stellar model (SCSM) using these new tables. We first manually calibrate the surface Z/X abundance to within one part in 100 of the solar value. Subsequently, we allow both the convective mixing length parameter, α_{ML} , and the initial Hydrogen mass fraction, X , to vary simultaneously, minimizing the difference, to within one part in 10^5 , between resultant models' final radius and luminosity to those of the sun. Finally, we confirm that the model's surface Z/X abundance is still within one part in 100 of the solar value.

Solar calibrated stellar models evolved using GS98 OPAL and OPLIB opacity tables (Figure 4) differ $\sim 0.5\%$ in the SCSM hydrogen mass fractions and $\sim 1.5\%$ in the SCSM convective mixing length parameters (Table 1). While the two evolutionary tracks are very similar, note that the OPLIB SCSM's luminosity is systematically lower past the solar age. While at the solar age the OPLIB SCSM luminosity is effectively the same as the OPAL SCSM. This luminosity difference between

¹ <https://aphysics2.lanl.gov/apps/>

² <https://github.com/tboudreux/pytopsscrape>

Model	X	α_{ML}
OPAL	0.7066	1.9333
OPLIB	0.7107	1.9629

Table 1. Optimized parameters for SCSMs evolved using OPAL and OPLIB high temperature opacity tables.

OPAL and OPLIB based models is not inconsistent with expectations given the more shallow radiative temperature gradient resulting from the lower OPLIB opacities

4. MODELING

In order to model the Jao Gap we evolve two extremely finely sampled mass grids of models. One of these grids uses the OPAL high-temperature opacity tables while the other uses the OPLIB tables (Figure 5). Each grid evolves a model every $0.00025 M_{\odot}$ from 0.2 to $0.4 M_{\odot}$ and every $0.005 M_{\odot}$ from 0.4 to $0.8 M_{\odot}$. All models in both grids use a GS98 solar composition, the (1, 101, 0) FreeEOS (version 2.7) configuration, and 1000 year old pre-main sequence polytropic models, with polytropic index 1.5, as their initial conditions.

Because in this work we are just interested in the location shift of the Gap as the opacity source varies, we do not model variations in composition. Mansfield & Kroupa (2021); Jao & Feiden (2020); Feiden et al. (2021) all look at the effect composition has on Jao Gap location. They find that as population metallicity increases so too does the mass range and consequently the magnitude of the Gap. From an extremely low metallicity population ($Z=0.001$) to a population with a more solar like metallicity this shift in mass range can be up to 0.05 M_{\odot} (Mansfield & Kroupa 2021).

4.1. Population Synthesis

In order to compare the Gap to observations we use in house population synthesis code. We empirically calibrate the relation between G, BP, and RP magnitudes and their uncertainties along with the parallax/G magnitude uncertainty relation using the Gaia Catalogue of Nearby Stars (GCNS, Gaia Collaboration et al. 2021) and Equations 3 & 4. M_g is the Gaia G magnitude while M_i is the magnitude in the i^{th} band, G, BP, or RP. The coefficients a , b , and c determined using a non-linear least squares fitting routine. Equation 3 then models the relation between G magnitude and parallax uncertainty while Equation 4 models the relation between each magnitude and its uncertainty.

$$\sigma_{plx}(M_g) = ae^{bM_g} + c \quad (3)$$

$$\sigma_i(M_i) = ae^{M_i - b} + c \quad (4)$$

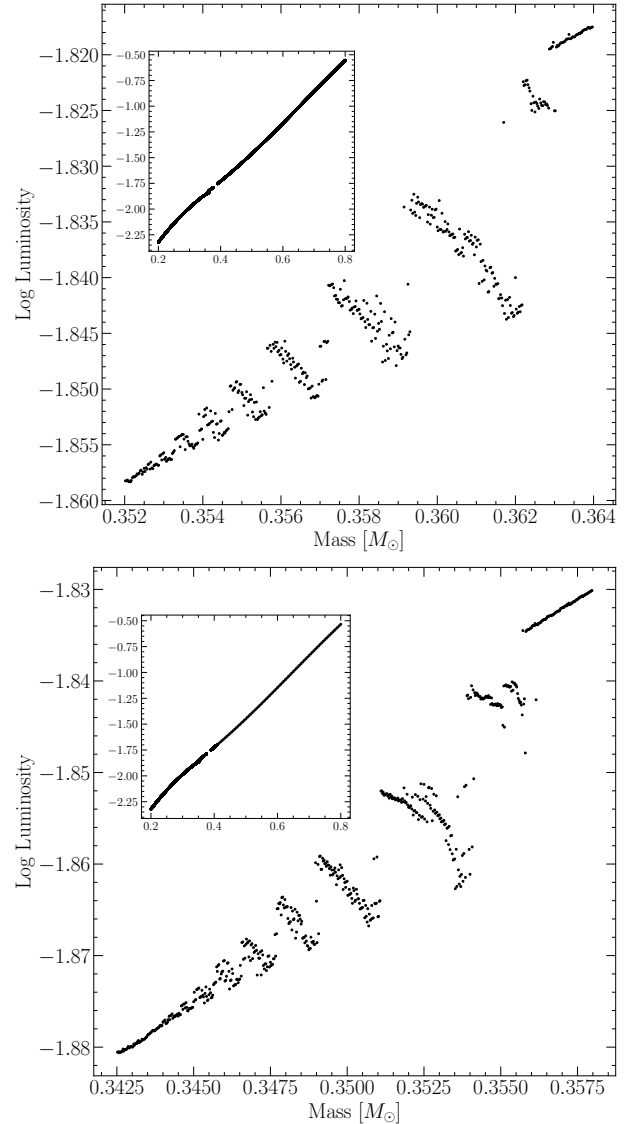


Figure 5. Mass-luminosity relation at 7 Gyrs for models evolved using OPAL opacity tables (top) and those evolved using OPLIB opacity tables (bottom). Note the lower mass range of the OPLIB Gap.

The full series of steps in our population synthesis code are:

1. Sample from a Sollima (2019) ($0.25M_{\odot} < M < 1M_{\odot}$, $\alpha = -1.34 \pm 0.07$) IMF to determine synthetic star mass.
2. Find the closest model above and below the synthetic star, linearly interpolate these models' T_{eff} , $\log(g)$, and $\log(L)$ to those at the synthetic star mass.
3. Convert synthetic star g , T_{eff} , and $\log(L)$ to Gaia G, BP, and RP magnitudes using the Gaia (E)DR3

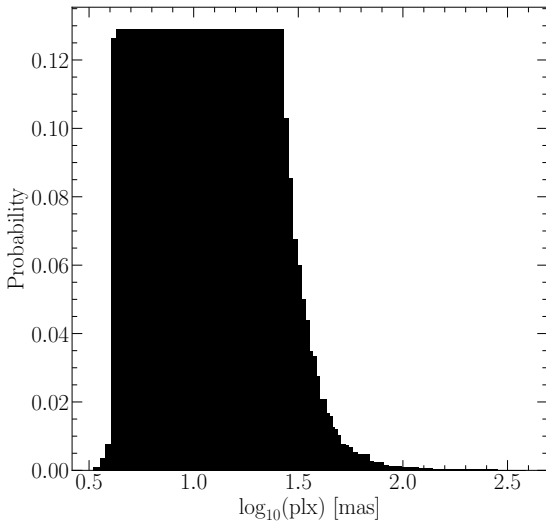


Figure 6. Probability distribution sampled when assigning true parallaxes to synthetic stars. This distribution is built from the GCNS and includes all stars with BP-RP colors between 2.3 and 2.9, the same color range of the Jao Gap.

308 bolometric corrections (Creevey et al. 2022) along
309 with code obtained thorough personal communica-
310 tion with Aaron Dotter (Choi et al. 2016).

- 311 4. Sample from the GCNS parallax distribution (Figure 6), limited to stars within the BP-RP color
312 range of 2.3 – 2.9, to assign synthetic star a “true”
313 parallax.
- 315 5. Use the true parallax to find an apparent magni-
316 tude for each filter.
- 317 6. Evaluate the empirical calibration given in Equa-
318 tion 3 to find an associated parallax uncertainty.
319 Then sample from a normal distribution with a
320 standard deviation equal to that uncertainty to
321 adjust the true parallax resulting in an “observed”
322 parallax.
- 323 7. Use the “observed” parallax and the apparent
324 magnitude to find an “observed” magnitude.
- 325 8. Fit the empirical calibration given in Equation 4
326 to the GCNS and evaluate it to give a magnitude
327 uncertainty scale in each band.
- 328 9. Adjust each magnitude by an amount sampled
329 from a normal distribution with a standard devi-
330 ation of the magnitude uncertainty scale found
331 in the previous step.

Model	Location	Prominence	Width
OPAL 1	10.138	0.593	0.027
OPAL 2	10.183	0.529	0.023
OPLIB 1	10.188	0.724	0.032
OPLIB 2	10.233	0.386	0.027

Table 2. Locations identified as potential Gaps.

332 This method then incorporates both photometric and
333 astrometric uncertainties into our population synthe-
334 sis. An example 7 Gyr old synthetic populations using
335 OPAL and OPLIB opacities are presented in Figure 7.

336 5. RESULTS

337 We quantify the Jao Gap location along the magni-
338 tude (Table 2) axis by sub-sampling our synthetic pop-
339 ulations, finding the linear number density along the
340 magnitude axis of each sub-sample, averaging these lin-
341 ear number densities, and extracting any peaks above
342 a prominence threshold of 0.1 as potential magnitudes
343 of the Jao Gap (Figure 8). Gap widths are measured
344 at 50% the height of the peak prominence. We use the
345 python package `scipy` (Virtanen et al. 2020) to both
346 identify peaks and measure their widths.

347 In both OPAL and OPLIB synthetic populations our
348 Gap identification method finds two gaps above the
349 prominence threshold. The identification of more than
350 one gap is not inconsistent with the mass-luminosity
351 relation seen in the grids we evolve. As noise is in-
352 jected into a synthetic population smaller features will
353 be smeared out while larger ones will tend to persist.
354 The mass-luminosity relations shown in in Figure 5 make
355 it clear that there are: (1), multiple gaps due to stars of
356 different masses undergoing convective mixing events at
357 different ages, and (2), the gaps decrease in width mov-
358 ing to lower masses / redder. Therefore, the multiple
359 gaps we identify are attributable to the two bluest gaps
360 being wide enough to not smear out with noise. In fact,
361 if we lower the prominence threshold just slightly from
362 0.1 to 0.09 we detect a third gap in both the OPAL and
363 OPLIB datasets where one would be expected.

364 Previous modeling efforts (e.g. Feiden et al. 2021) have
365 not identified multiple gaps. This is likely due to two
366 reasons: (1), previous studies have allowed metallicity to
367 vary across their model grids, further smearing the gaps
368 out, and (2), previous studies have used more coarse
369 underlying mass grids, obscuring features smaller than
370 their mass step. While this dual-gap structure has not
371 been seen in models before, a more complex gap struc-
372 ture is not totally unprecedented as Jao & Feiden (2021)
373 identifies an additional under-dense region below the pri-
374 mary gap in EDR3 data. As part of a follow up series

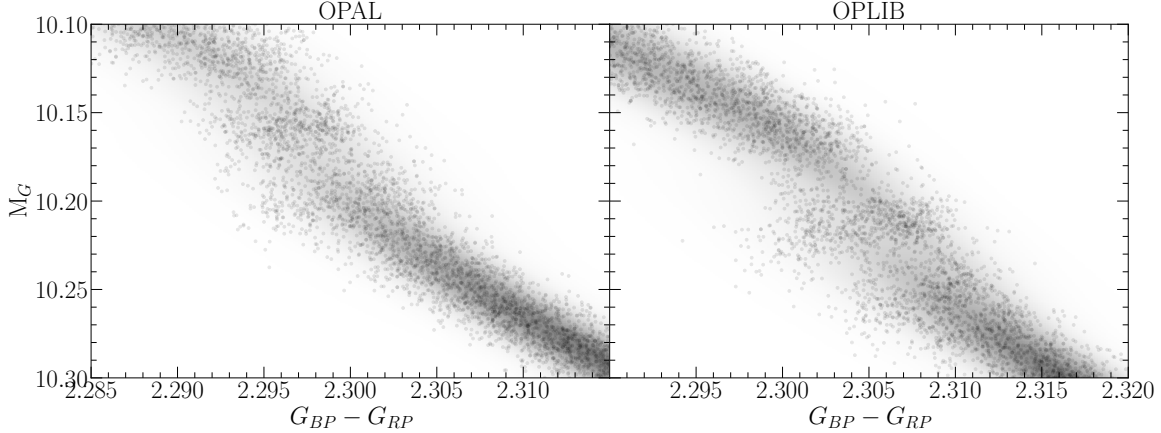


Figure 7. Population synthesis results for models evolved with OPAL (left) and models evolved with OPLIB (right). A Gaussian kernel-density estimate has been overlaid to better highlight the density variations.

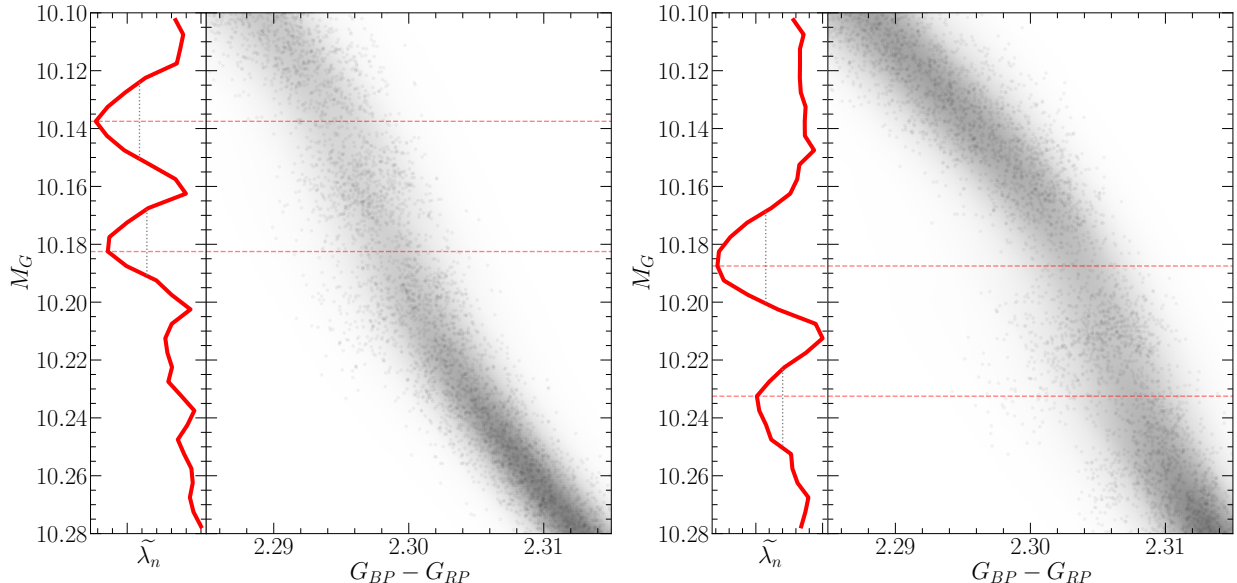


Figure 8. (right panels) OPAL (left) and OPLIB (right) synthetic populations. (left panels) Normalized linear number density along the magnitude axis. A dashed line has been extended from the peak through both panels to make clear where the identified Jao Gap location is wrt. to the population.

375 of papers, we are conducting further work to incorporate
376 rate metallicity variations while still using the finer mass
377 sampling presented here.

378 The mean gap location of the OPLIB population is at
379 a fainter magnitude than the mean gap location of the
380 OPAL population. Consequently, in the OPLIB sample
381 the convective mixing events which drive the kissing in-
382 stability begin happening at lower masses (i.e. the con-
383 vective transition mass decreases). A lower mass range
384 will naturally result in a fainter mean gap magnitude.

385 Mixing events at lower masses in OPLIB models are
386 attributable to the radially thicker, at the same mass,
387 radiative zones (Figure 9). This thicker radiative zone
388 will take more time to break down and is characteristic

389 of OPLIB models as of a result of their slightly lower
390 opacities. A lower opacity fluid will have a more shal-
391 low radiative temperature gradient than a higher opac-
392 ity fluid; however, as the adiabatic temperature gradient
393 remains essentially unchanged as a function of radius, a
394 larger interior radius of the model will remain unsta-
395 ble to radiation. This thicker radiative zone will in-
396 crease the time it takes the core convective zone to meet
397 up with convective envelope meaning that lower mass
398 models can sustain a radiative zone for longer than they
399 could otherwise; thus; lower opacities push the convec-
400 tive transition mass down. We can additionally see this
401 longer lived radiative zone in the core ^3He mass fraction,
402 in which OPLIB models reach much higher concentra-

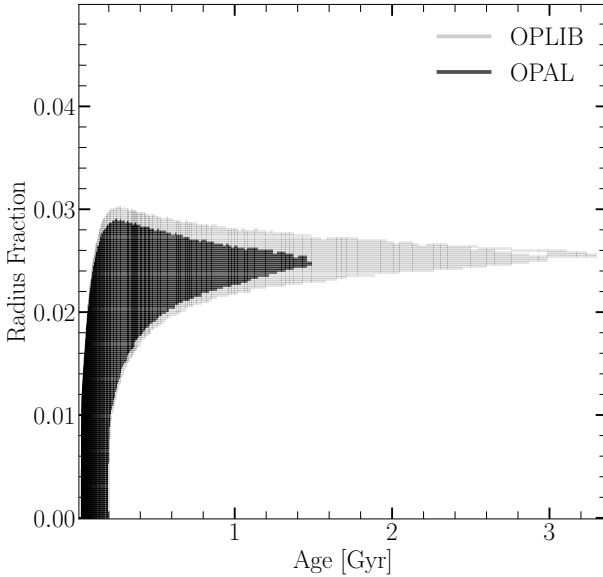


Figure 9. Portions of $0.3526 M_{\odot}$ OPAL and OPLIB stellar models showing the interior shells which are radiative (black region). Note that for clarity only one convective mixing event from each model is shown. Note how the radiative zone in the OPLIB model is larger.

tions — at approximately the same growth rate — for the same mass as OPAL models do (Figure 10).

The most precise published Gap location comes from Jao & Feiden (2020) who use EDR3 to locate the Gap at $M_G \sim 10.3$, we identify the Gap at a similar location in the GCNS data. **The Gap in populations evolved using OPLIB tables is closer to this measurement than it is in populations evolved using OPAL tables (Table 2).** It should be noted that the exact location of the observed Gap is poorly captured by a single value as the Gap visibly compresses across the width of the main-sequence, wider on the blue edge and narrower on the red edge such that the observed Gap has downward facing a wedge shape (Figure 1). This wedge shape is not successfully reproduced by either any current models or the modeling we perform here. We elect then to specify the Gap location where this wedge is at its narrowest, on the red edge of the main sequence.

The Gaps identified in our modeling have widths of approximately 0.03 magnitudes, while the shift from OPAL to OPLIB opacities is 0.05 magnitudes. With the prior that the Gaps clearly shift before noise is injected we know that this shift is real. However, the shift magnitude and Gap width are of approximately the same size in our synthetic populations. Moreover, Feiden et al. (2021) identify that the shift in the mod-

eled Gap mass from $[Fe/H] = 0$ to $[Fe/H] = +0.5$ as $0.04 M_{\odot}$, whereas we only see an approximate $0.01 M_{\odot}$ shift between OPAL and OPLIB models. Therefore,

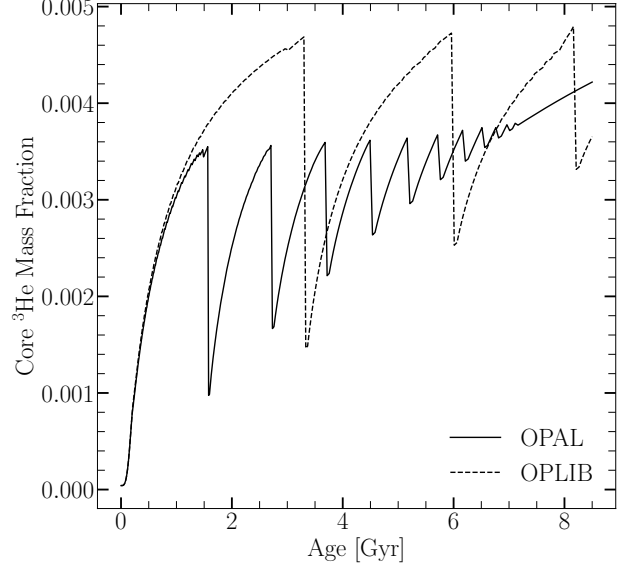


Figure 10. Core ${}^3\text{He}$ mass fraction for $0.3526 M_{\odot}$ models evolved with OPAL and OPLIB (within the Jao Gap's mass range for both). Note how the OPLIB model's core ${}^3\text{He}$ mass fraction grows at approximately the same rate as the OPAL model's but continues uninterrupted for longer.

the Gap location will likely not provide a usable constraint on the opacity source.

6. CONCLUSION

The Jao Gap provides an intriguing probe into the interior physics of M Dwarfs stars where traditional methods of studying interiors break down. However, before detailed physics may be inferred it is essential to have models which are well matched to observations. Here we investigate whether the OPLIB opacity tables reproduce the Jao Gap location and structure more accurately than the widely used OPAL opacity tables. We find that while the OPLIB tables do shift the Jao Gap location more in line with observations, by approximately 0.05 magnitudes, the shift is small enough that it is likely not distinguishable from noise due to population age and chemical variation. However, future measurement of $[Fe/H]$ for stars within the gap will be helpful in constraining the degree to which the gap should be smeared by these theoretical models. Finally, we do not find that the OPLIB opacity tables help in reproducing the as yet unexplained wedge shape of the observed Gap.

454

A. PYTOPSSCRAPE

455 pyTOPSScrape provides an easy to use command line and python interface for the OPLIB opacity tables accessed
 456 through the TOPS web form. Extensive documentation of both the command line and programmatic interfaces is
 457 linked in the version controlled repository. However, here we provide a brief, illustrative, example of potential use.

458 Assuming pyTOPSScrape has been installed and given some working directory which contains a file describing a base
 459 composition (“comp.dat”) and another file containing a list of rescalings of that base composition (“rescalings.dat”)
 460 (both of these file formats are described in detail in the documentation), one can query OPLIB opacity tables and
 461 convert them to a form mimicking that of type 1 OPAL high temperature opacity tables using the following shell
 462 command.

463 \$ generateTOPStables comp.dat rescalings.dat -d ./TOPSCache -o out.opac -j 20

464 For further examples of pyTOPSScrape please visit the repository.

465

B. INTERPOLATING $\rho \rightarrow R$

466 OPLIB parameterizes κ_R as a function of mass density, temperature in keV, and composition. Type 1 OPAL high
 467 temperature opacity tables, which DSEP and many other stellar evolution programs use, instead parameterizes opacity
 468 as a function of temperature in Kelvin, R (Equation B1), and composition. The conversion from temperature in keV
 469 to Kelvin is trivial (Equation B2).

$$470 \quad 471 \quad 472 \quad R = \frac{\rho}{T_6^3} \quad (B1)$$

$$473 \quad 474 \quad T_K = T_{keV} * 11604525.0061657 \quad (B2)$$

475 However, the conversion from mass density to R is more involved. Because R is coupled with both mass density and
 476 temperature there is no way to directly convert tabulated values of opacity reported in the OPLIB tables to
 477 their equivalents in R space. Instead we must rotate the tables, interpolating $\kappa_R(\rho, T_{eff}) \rightarrow \kappa_R(R, T_{eff})$.

478 To perform this rotation we use the `interp2d` function within `scipy`’s `interpolate` (Virtanen et al. 2020) module to
 479 construct a cubic bivariate B-spline (Dierckx 1981) interpolating function s , with a smoothing factor of 0, representing
 480 the surface $\kappa_R(\rho, T_{eff})$. For each R^i and T_{eff}^j reported in type 1 OPAL tables, we evaluate Equation B1 to find
 481 $\rho^{ij} = \rho(T_{eff}^j, R^i)$. Opacities in T_{eff} , R space are then inferred as $\kappa_R^{ij}(R^i, T_{eff}^j) = s(\rho^{ij}, T_{eff}^j)$.

482 As first-order validation of this interpolation scheme we can perform a similar interpolation in the opposite direction,
 483 rotating the tables back to $\kappa_R(\rho, T_{eff})$ and then comparing the initial, “raw”, opacities to those which have gone
 484 through the interpolations process. Figure 11 shows the fractional difference between the raw opacities and a set
 485 which have gone through this double interpolation. The red line denotes $\log(R) = -1.5$ where models will tend to sit
 486 for much of their radius. Along the $\log(R) = -1.5$ line the mean fractional difference is $\langle \delta \rangle = 0.006$ with an uncertainty
 487 of $\sigma_{\langle \delta \rangle} = 0.009$. One point of note is that, because the initial rotation into $\log(R)$ space also reduces the domain of the
 488 opacity function, interpolation-edge effects which we avoid initially by extending the domain past what type 1 OPAL
 489 tables include cannot be avoided when interpolating back into ρ space.

490 This work has made use of the NASA astrophysical data system (ADS). We would like to thank Elisabeth Newton,
 491 Aaron Dotter, and Gregory Feiden for their support and for useful discussion related to the topic of this paper.
 492 Additionally, we would like to thank James Colgan and the Los Alamos T-1 group for their assistance with the OPLIB
 493 opacity tables and support for the public release of pyTOPSScrape. We acknowledge the support of a NASA grant
 494 (No. 80NSSC18K0634).

495 *Software:* The Dartmouth Stellar Evolution Program (DSEP) (Dotter et al. 2008), BeautifulSoup (Richardson
 496 2007), mechanize (Chandra & Varanasi 2015), FreeEOS (Irwin 2012), pyTOPSScrape (Boudreux 2022)

REFERENCES

- 497 Amard, L., Palacios, A., Charbonnel, C., et al. 2019, A&A, 631, A77, doi: 10.1051/0004-6361/201935160
- 499 Bahcall, J. N., Serenelli, A. M., & Basu, S. 2005, ApJL, 621, L85, doi: 10.1086/428929
- 500

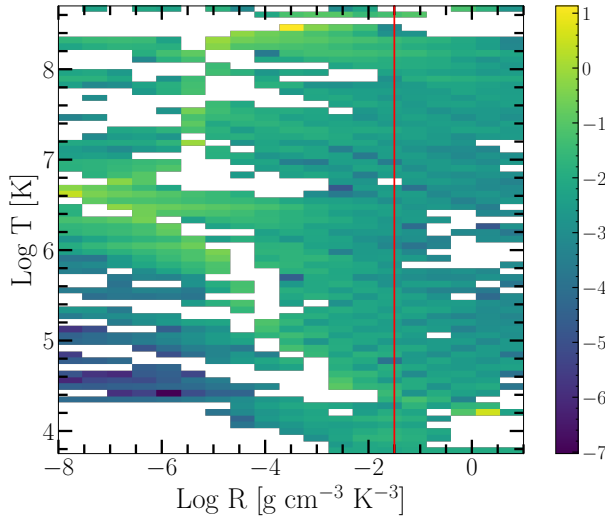


Figure 11. Log Fractional Difference between opacities in $\kappa_R(\rho, T_{eff})$ space directly queried from the OPLIB web-form and those which have been interpolated into $\log(R)$ space and back. Note that, due to the temperature grid of type 1 OPAL tables not aligning perfectly with the temperature grid OPLIB uses there may be edge effects where the interpolation is poorly constrained. The red line corresponds to $\log(R) = -1.5$ where much of a stellar model's radius exists.

- 501 Baraffe, I., & Chabrier, G. 2018, A&A, 619, A177,
502 doi: [10.1051/0004-6361/201834062](https://doi.org/10.1051/0004-6361/201834062)
- 503 Boudreault, T. 2022, tboudreault/pytopsscrape:
504 pyTOPSScrape v1.0, v1.0, Zenodo,
505 doi: [10.5281/zenodo.7094198](https://doi.org/10.5281/zenodo.7094198)
- 506 Chabrier, G., & Baraffe, I. 1997, A&A, 327, 1039.
507 <https://arxiv.org/abs/astro-ph/9704118>
- 508 Chandra, R. V., & Varanasi, B. S. 2015, Python requests
509 essentials (Packt Publishing Ltd)
- 510 Choi, J., Dotter, A., Conroy, C., et al. 2016, ApJ, 823, 102,
511 doi: [10.3847/0004-637X/823/2/102](https://doi.org/10.3847/0004-637X/823/2/102)
- 512 Colgan, J., Kilcrease, D. P., Magee, N. H., et al. 2016, in
513 APS Meeting Abstracts, Vol. 2016, APS Division of
514 Atomic, Molecular and Optical Physics Meeting
515 Abstracts, D1.008
- 516 Creevey, O. L., Sordo, R., Paillet, F., et al. 2022, arXiv
517 e-prints, arXiv:2206.05864.
518 <https://arxiv.org/abs/2206.05864>
- 519 Dierckx, P. 1981, IMA Journal of Numerical Analysis, 1,
520 267, doi: [10.1093/imanum/1.3.267](https://doi.org/10.1093/imanum/1.3.267)
- 521 Dotter, A., Chaboyer, B., Jevremović, D., et al. 2008, The
522 Astrophysical Journal Supplement Series, 178, 89
- 523 Feiden, G. A., Skidmore, K., & Jao, W.-C. 2021, ApJ, 907,
524 53, doi: [10.3847/1538-4357/abcc03](https://doi.org/10.3847/1538-4357/abcc03)
- 525 Ferguson, J. W., Alexander, D. R., Allard, F., et al. 2005,
526 ApJ, 623, 585, doi: [10.1086/428642](https://doi.org/10.1086/428642)
- 527 Fontes, C. J., Zhang, H. L., Abdallah, J. J., et al. 2015,
528 Journal of Physics B Atomic Molecular Physics, 48,
529 144014, doi: [10.1088/0953-4075/48/14/144014](https://doi.org/10.1088/0953-4075/48/14/144014)
- 530 Gaia Collaboration, Smart, R. L., Sarro, L. M., et al. 2021,
531 A&A, 649, A6, doi: [10.1051/0004-6361/202039498](https://doi.org/10.1051/0004-6361/202039498)
- 532 Hakel, P., Sherrill, M. E., Mazevet, S., et al. 2006, JQSRT,
533 99, 265, doi: [10.1016/j.jqsrt.2005.04.007](https://doi.org/10.1016/j.jqsrt.2005.04.007)
- 534 Iglesias, C. A., & Rogers, F. J. 1996, ApJ, 464, 943,
535 doi: [10.1086/177381](https://doi.org/10.1086/177381)
- 536 Irwin, A. W. 2012, FreeEOS: Equation of State for stellar
537 interiors calculations, Astrophysics Source Code Library,
538 record ascl:1211.002. <http://ascl.net/1211.002>
- 539 Jao, W.-C., & Feiden, G. A. 2020, AJ, 160, 102,
540 doi: [10.3847/1538-3881/aba192](https://doi.org/10.3847/1538-3881/aba192)
- 541 —. 2021, Research Notes of the American Astronomical
542 Society, 5, 124, doi: [10.3847/2515-5172/ac053a](https://doi.org/10.3847/2515-5172/ac053a)
- 543 Jao, W.-C., Henry, T. J., Gies, D. R., & Hambly, N. C.
544 2018, ApJL, 861, L11, doi: [10.3847/2041-8213/aacdf6](https://doi.org/10.3847/2041-8213/aacdf6)
- 545 MacDonald, J., & Gizis, J. 2018, MNRAS, 480, 1711,
546 doi: [10.1093/mnras/sty1888](https://doi.org/10.1093/mnras/sty1888)
- 547 Magee, N. H., Abdallah, J., Colgan, J., et al. 2004, in
548 American Institute of Physics Conference Series, Vol.
549 730, Atomic Processes in Plasmas: 14th APS Topical
550 Conference on Atomic Processes in Plasmas, ed. J. S.
551 Cohen, D. P. Kilcrease, & S. Mazavet, 168–179,
552 doi: [10.1063/1.1824868](https://doi.org/10.1063/1.1824868)
- 553 Mansfield, S., & Kroupa, P. 2021, A&A, 650, A184,
554 doi: [10.1051/0004-6361/202140536](https://doi.org/10.1051/0004-6361/202140536)
- 555 Nutzman, P., & Charbonneau, D. 2008, PASP, 120, 317,
556 doi: [10.1086/533420](https://doi.org/10.1086/533420)
- 557 Richardson, L. 2007, April
- 558 Rodríguez-López, C. 2019, Frontiers in Astronomy and
559 Space Sciences, 6, 76, doi: [10.3389/fspas.2019.00076](https://doi.org/10.3389/fspas.2019.00076)

- ⁵⁶⁰ Seaton, M. J., Yan, Y., Mihalas, D., & Pradhan, A. K.
⁵⁶¹ 1994, MNRAS, 266, 805, doi: [10.1093/mnras/266.4.805](https://doi.org/10.1093/mnras/266.4.805)
- ⁵⁶² Skrutskie, M. F., Cutri, R. M., Stiening, R., et al. 2006, AJ,
⁵⁶³ 131, 1163, doi: [10.1086/498708](https://doi.org/10.1086/498708)
- ⁵⁶⁴ Sollima, A. 2019, Monthly Notices of the Royal
⁵⁶⁵ Astronomical Society, 489, 2377,
⁵⁶⁶ doi: [10.1093/mnras/stz2093](https://doi.org/10.1093/mnras/stz2093)
- ⁵⁶⁷ van Saders, J. L., & Pinsonneault, M. H. 2012, ApJ, 751,
⁵⁶⁸ 98, doi: [10.1088/0004-637X/751/2/98](https://doi.org/10.1088/0004-637X/751/2/98)
- ⁵⁶⁹ Virtanen, P., Gommers, R., Oliphant, T. E., et al. 2020,
⁵⁷⁰ Nature Methods, 17, 261, doi: [10.1038/s41592-019-0686-2](https://doi.org/10.1038/s41592-019-0686-2)